

FEDSM-ICNMM2010-00000

HYDROELASTIC RESPONSES OF A FLEXIBLE HYDROFOIL IN TURBULENT, CAVITATING FLOW

Antoine Ducoin & Yin Lu Young*

University of Michigan,
Dept. of Naval Arch. & Marine Eng., 2600 Draper Dr,
48109 Ann Arbor, Michigan, USA
Email: aducoin@umich.edu, ylyoung@umich.edu

Jean-François Sigrist

DCNS Propulsion
44620, La Montagne
France
Email: jean-francois.sigrist@dcnsgroup.com

ABSTRACT

The objective of this work is to develop and validate a robust method to simulate the hydroelastic responses of flexible hydrofoil in turbulent, cavitating flow. A two degrees-of-freedom (2-DOF) model is used to simulate the plunging and pitching motion at the foil tip due to bending and twisting deformation of a 3-D cantilevered hydrofoil. The 2-DOF model is loosely coupled with the commercial computational fluid dynamics (CFD) solver STAR-CCM+ to efficiently simulate the fluid-structure interaction (FSI) responses of a cantilevered, rectangular hydrofoil. The numerical predictions are compared with experimental measurements for cases with and without cavitation. The experimental studies were conducted in the cavitation tunnel at the French Naval Academy (IRENav), France. Only quasi-steady cases with Reynolds number (Re) of 750,000 are shown in this paper. In general, the numerical results agree well with the experimental measurements and observations. The results show that elastic deformation of the POM polyacetate (flexible) hydrofoil lead to increases in the angle of attack, which resulted in higher lift and drag coefficients, lower lift to drag ratio, and longer cavities compared to the stainless steel (rigid) hydrofoil. Whereas only stable cavitation cases are considered in this paper, significant interaction effects were observed during experiments for cases with unstable cavitation due to interactions between the foil natural frequencies and the cavity shedding frequencies. Transient analysis of the FSI responses of 3-D elastic hydrofoils in turbulent, cavitating flow is currently under work.

1 Introduction

The objective of this work is to develop and validate a robust method to simulate the hydroelastic responses of flexible hydrofoil in turbulent, cavitating flow. Such flow conditions exist for many types of marine structures, including hydrofoils, propellers, rudders, turbines, etc, particularly when operating at off-design conditions. Although much work exist on the study of the cavitating response of rigid hydrofoils through experimental (e.g. [1], [2], [3], [4], [5]) and numerical studies ([6], [7]), only limited studies have been conducted on flexible hydrofoils. In Gowing et al. 1998 [8], experimental results for a composite elliptic hydrofoil showed that hydrodynamic-load induced tip deflections helped to delay cavitation inception without changing the overall lift and drag coefficients. Recent works of Young 2008 [9] and Motley et al. 2009 [10] on self-adaptive composite marine propellers showed noticeable improvements in propulsive efficiency and cavitating performance via the use of composite materials by tailoring the anisotropic, elastic deformations. A theoretical study by Amromin and Kovinskaia (2000) [11] focused on the vibration of an elastic hydrofoil with an attached cavity in periodically perturbed flow. Hydrofoil vibration was described by means of a beam equation. The results showed a global increase of the structural vibrations due to cavitation, where a high frequency band is associated to the hydrofoil natural frequencies, and a low frequency band is associated to cavity volume fluctuations. Although some advances have been made to advance the understanding of the FSI responses of cavitating hydrofoils, more work is needed, particularly concerning flexible

*Address all correspondence to this author.

Nomenclature

b	hydrofoil span
c	hydrofoil chord
C_D	drag coefficient ($C_D = \frac{D}{0.5\rho_l V_\infty^2 S}$)
C_L	lift coefficient ($C_L = \frac{L}{0.5\rho_l V_\infty^2 S}$)
C_P	pressure coefficient ($C_P = \frac{P - P_\infty}{0.5\rho_l V_\infty^2}$)
D	drag
h	bending DOF at the foil tip
K_h	bending stiffness
K_θ	torsional stiffness
L	lift force
P	local pressure
P_v	vapor pressure
P_∞	reference pressure
Re	Reynolds number ($Re = \frac{V_\infty c}{\nu_l}$)
S	projected hydrofoil surface area ($S = c \times b$)
T	torque (axial moment)
$\vec{u} = (u, v)$	local fluid velocity vector
V_∞	free stream horizontal velocity
\vec{X}_E	elastic axis
\vec{X}_P	center of pressure
y^+	dimensionless wall distance ($y^+ = \frac{y \rho_F \mu_\tau}{\mu_F}$)
α	angle of incidence
α_v	volume fraction of vapor
μ_F	dynamic mixture viscosity
μ_l	dynamic water viscosity
μ_v	dynamic vapor viscosity
ν_l	kinematic water viscosity
θ	pitch DOF at the foil tip
ρ_F	fluid mixture density
ρ_l	water density
ρ_s	structure density
ρ_v	vapor density
σ	cavitation number ($\sigma = \frac{P_\infty - P_v}{0.5\rho_l V_\infty^2}$)

hydrofoils in turbulent flows.

1.1 Objective

The objective of this work is to develop and validate a robust method to simulate the hydroelastic responses of a flexible hydrofoil in turbulent, cavitating flow. A similar work which focused on the subcavitating (fully wetted) responses of a flexible hydrofoil can be found in Ducoin et al 2009 [12].

1.2 Organization

This paper is organized as follows. First, a summary of the numerical model is presented in Section 2, which includes the

fluid model (Section 2.1), the solid model (Section 2.2), numerical setup and boundary conditions (Section 2.3), and the FSI coupling algorithm (Section 2.4). A summary of the experimental model for both a rigid and a flexible hydrofoil is presented in Section 3. Comparisons of numerical predictions with experimental measurements are shown in Section 4. Finally, the conclusions are presented in Section 5.

2 Numerical Model

In this work, the hydrodynamic response of a flexible hydrofoil is simulated using the commercial CFD solver STAR-CCM+; the plunging and pitching motion at the foil tip due to bending and twisting deformation (of the 3-D cantilevered hydrofoil) is simulated using a 2-DOF model. The fluid and solid solvers are coupled via a user-defined subroutine in STAR-CCM+, which exchanges the fluid pressure field and foil motions between the solvers. A summary of the fluid model, solid model, numerical setup and boundary conditions, and FSI coupling algorithm are presented below.

2.1 Fluid Model

The fluid problem is solved with a finite volume technique using the commercial CFD code STAR-CCM+. The vapor-liquid flow is assumed to be a homogenous, isothermal, two-phase flow governed by the variable density Reynolds-Averaged Navier Stokes (RANS) equations. The Spalart-Allmaras ([13]) model is used for the turbulence modeling. It is a one-equation model where the eddy viscosity transport equation is given as:

$$\frac{\partial}{\partial t} (\rho_F \tilde{v}) + \nabla \cdot (\rho_F \vec{u} \tilde{v}) = \rho_F C_{b1} \tilde{S} \tilde{v} + \frac{1}{c_v} \left[\nabla \cdot ((\mu_F + \rho_F \tilde{v}) \nabla \tilde{v}) + \rho_F C_{b2} |\nabla \tilde{v}|^2 \right] - \rho_F C_{w1} f_w \left(\frac{\tilde{v}}{d} \right)^2 \quad (1)$$

where \vec{u} is the local fluid velocity vector and \tilde{v} is the transported quantity, which is related to the turbulent viscosity, μ_t :

$$\mu_t = \rho_F \tilde{v} f_{v1} \quad (2)$$

where f_{v1} is a viscous damping function which is used to ensure that $\tilde{v} = \kappa d u_\tau$ in the log layer, the buffer layer and the viscous sublayer. κ is called the von Karman constant and u_τ is the friction velocity. The function f_{v1} can be written as :

$$f_{v1} = \frac{\chi^3}{\chi^3 + C_{v1}^3} \quad (3)$$

where χ is the ratio between the working variable and the laminar viscosity, and C_{v1} is a model constant.

The variable d in Eq. 1 is the distance to the closest wall and \tilde{S} is a transformed vorticity which maintains the vorticity log layer behavior. C_{b1}, C_{b2}, C_{w1} , and c_v are model constants. The two first terms in the right-hand-side of Eq. 1 represent the production and destruction of turbulent viscosity, respectively. The last term of Eq. 1 represents the turbulent diffusion. The function f_w is used in order to obtain a faster decaying behavior of destruction in the outer region of the boundary layer; f_w is equal to 1 in the log layer, and decreases in the outer region.

Additional details about the Spalart-Allmaras turbulence model and the model constants can be found in Spalart et Allmaras [13]. This model has been shown to be reliable for cavitating flows [14]. A systematic numerical study by the authors using the same fluid solver and same grid has shown that the results (lift and drag coefficients, and cavity length) obtained using the Spalart-Allmaras model ([13]) compared better with the experimental measurements than the results obtained using the $k-\epsilon$ ([15]) and $k-\omega$ SST ([16]) models.

The density and the dynamic viscosity (ρ_F and μ_F) of the fluid mixture are expressed as functions of the vapor density and viscosity (ρ_v, μ_v), liquid density and viscosity (ρ_l, μ_l), and volume fraction of vapor (α_v):

$$\rho_F = \alpha_v \cdot \rho_v + (1 - \alpha_v) \cdot \rho_l \quad (4)$$

$$\mu_F = \alpha_v \cdot \mu_v + (1 - \alpha_v) \cdot \mu_l \quad (5)$$

In these equations, the density and viscosity of the individual vapor and liquid phases are assumed to be constants, but the mixture density and viscosity are allowed to vary spatially and temporally with changes in α_v .

The cavitation model follows Scherr & Sauer 2001 [17], which is a single fluid model for a homogeneous vapor-liquid mixture consists, and is formulated based on bubble dynamics. The relationship between the vapor volume fraction α_v and the vapor bubble radius R is given by:

$$\alpha_v = \frac{V_V}{V} = \frac{n_0 \frac{4}{3} \pi R^3}{1 + n_0 \frac{4}{3} \pi R^3} \quad (6)$$

where n_0 is the bubble density per cubic meter, V is the cell volume and V_V is the volume of vapor in that cell. The bubbles are assumed to be purely spherical and the effect of bubble-bubble interactions are ignored.

The change in bubble radius (R) with time (t) is given by the Rayleigh-Plesset equation:

$$R \frac{d^2 R}{dt^2} + \frac{3}{2} \left(\frac{dR}{dt} \right)^2 = \frac{P_B - P_\infty}{\rho_l} - \frac{2s_t}{\rho_l R} - 4 \frac{\mu_l}{\rho_l R} \frac{dR}{dt} \quad (7)$$

where P_B is the fluid pressure at the bubble boundary, which is equal to the vapor pressure P_v , and s_t is the surface tension coefficient. P_∞ is the reference pressure.

The transport equation is solved in order to determine the instantaneous volume fraction α_v of each cell:

$$\frac{\partial \alpha_v}{\partial t} + \nabla \cdot (\alpha_v \vec{u}) = \frac{n_0}{1 + n_0 \frac{4}{3} \pi R^3} \cdot \frac{d}{dt} \left(\frac{4}{3} \pi R^3 \right) \quad (8)$$

2.2 Solid Model

The plunging and pitching motion at the foil tip caused by spanwise bending and twisting of the 3-D hydrofoil are represented using a 2-DOF model, as shown in Figure 1. The 2-D foil section is assumed to be located at an initial angle of attack α from the uniform inflow in the x -direction. The 2-D foil section is only allowed to undergo equivalent rigid body translation in the vertical direction (h) and rotation (θ) defined about the elastic axis, $\vec{X}_E = (x_E, y_E)$. The resulting lift (L) and drag (D) forces on the foil are applied at the center of pressure, $\vec{X}_P = (x_P, y_P)$, which is defined as follows:

$$\vec{X}_P = \frac{\int_0^c \vec{x} \times P(\vec{x}) d\vec{x}}{\int_0^c P(\vec{x}) d\vec{x}} \quad (9)$$

where c is the chord length, P is the local wall pressure, and $\vec{x} = (x, y)$ is the position vector. It should be noted that α is defined positive in the clockwise direction while θ is defined positive in the counter-clockwise direction.

The steady-state equations governing the simplified 2-DOF system can be written as:

$$K_h h = L \quad (10)$$

$$K_\theta \theta = T = L(y_E - y_P) + D(x_E - x_P) \quad (11)$$

where L and T represent the resultant total lift force and twisting moment, respectively, acting on the hydrofoil. K_h and K_θ are respectively the bending and torsional stiffnesses of the foil defined about the elastic axis.

2.3 Numerical Setup and Boundary Conditions

To demonstrate and validate the numerical model, results are shown for a cantilevered rectangular hydrofoil. The foil has a NACA 66 thickness distribution with a maximum thickness to chord ratio of 12%, and a NACA a = 0.8 camber distribution with a maximum camber to chord ratio of 2%. The chord length is $c = 0.15$ m and the span length is $b = 0.191$ m. All the results shown in this paper corresponds to the hydrofoil held fixed in place at its root inside a water tunnel (shown in Section 3) and subject

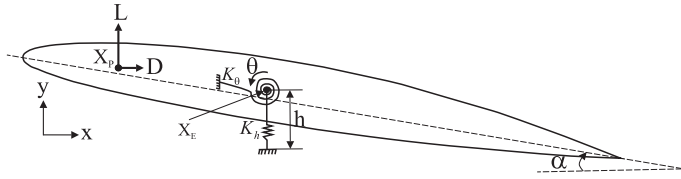


Figure 1. A 2-DOF model representing plunging (h) and pitching (θ) degrees of freedom at the tip of a cantilevered, rectangular hydrofoil.

to a nominal free stream velocity of $V_\infty = 5$ m/s, which yields a moderate to high Reynolds number of $Re = V_\infty c / \nu_l = 0.75 \times 10^6$.

The density and dynamic viscosity of the liquid are taken to be $\rho_l = 999.19$ kg/m³ and $\mu_l = \nu_l \rho_l = 1.139$ Pa·s, respectively, which correspond to fresh water at 15°C. The vapor density is $\rho_v = 0.595$ kg/m³ and the vapor viscosity is $\mu_v = 1.139$ Pa·s. The vapor pressure for water at 15°C is $P_v = 17000$ Pa. The average bubble radius is assumed to be $R = 10$ μm and the average bubble density $n_0 = 10^{11}$ bubbles per m³. The 2-D fluid domain is shown in Figure 2, which corresponds to the experimental test section shown in the next section. The distances between the elastic axis and the upstream and downstream boundaries are respectively $5.474c$ and $9.526c$; The distance between the elastic axis and top and bottom boundaries are respectively equal to $0.633c$ and $0.664c$. A no-slip boundary condition is imposed on the hydrofoil surface and symmetry conditions are imposed on the top and bottom boundaries of the tunnel. The inlet velocity is set to be $V_\infty = 5$ m/s and the outlet reference pressure is set to vary according to the cavitation number, defined as $\sigma = (P_\infty - P_v) / (0.5 \rho_l V_\infty^2)$. A constant turbulent intensity of 2% is set at the inlet and outlet boundaries and is equal to the experimentally measured turbulent intensity. All cavitating runs are initialized with a steady-state calculation using a high-pressure level in order to avoid any vapor fraction at the initial time step. The pressure is then decreased progressively until the specific cavitation number is reached. Only 2-D results are shown in this work. The 2-D fluid mesh (shown in Figure 2) is composed of 126,021 elements, with 50 structured elements across the boundary layer, which is selected to ensure $y^+ < 2$. The regions outside the boundary layer are discretized with polyhedral elements. Mesh refinements are performed at the foil leading edge, trailing edge, and in the wake region.

Second order schemes are used in all the fluid computations. The time integrator scheme is a second order backward Euler scheme, and the spatial derivatives are computed using a second order upwind scheme. Mesh convergence study has been conducted for the case of a fixed, rigid hydrofoil at an angle of attack of $\alpha = 6^\circ$ in steady, subcavitating (fully wetted, $\sigma = 7$) flow condition. The convergence of the lift ($C_L = L / 0.5 \rho_l V_\infty^2 S$) and drag ($C_D = D / 0.5 \rho_l V_\infty^2 S$) coefficients with number of elements are shown in Table 1, where S is the projected surface area of the hydrofoil defined as $S = c \times b$. It should be noted that for all

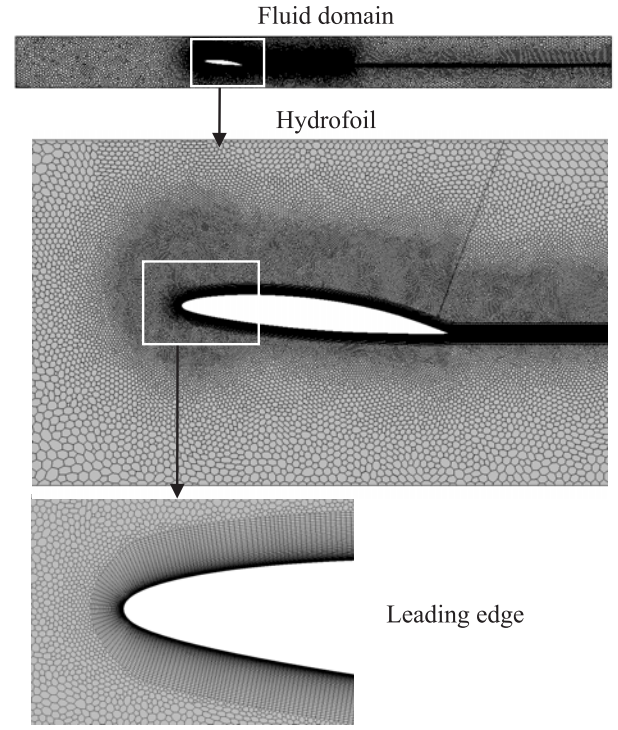


Figure 2. 2D finite volume mesh of the fluid domain.

the cases, the boundary layer mesh has a constant y^+ (first cell in contact with the hydrofoil) and thickness. The number of elements along the foil chord increases with mesh density. N_{foil} is the number of elements on the hydrofoil surface and N_{total} is the total number of elements in the fluid domain. Although the test case is for steady flow conditions, the full unsteady RANS equations are solved with a time step size of $\Delta t_f = 0.0001$ s, and the solution (lift and drag coefficients) corresponds to the values when steady-state is reached. The error for the lift and drag coefficients, shown in % in Table 1, are defined with respect to the finest mesh. The results show that the lift coefficient converges very fast, but a minimum of 200 elements are needed along the chord to reach convergence for the drag coefficient. For cavitating simulations, a finer mesh is needed to obtain a good description of the cavity. Hence, $N_{foil} = 400$ is used from herein for all computations.

The effect of time step size is shown for the case of a fixed, rigid hydrofoil at an angle of attack of $\alpha = 6^\circ$ in steady, cavitating flow with $\sigma = 1.49$. The convergence of the steady-state lift and drag coefficients, and the corresponding upper and lower bounds, with time step size, Δt_f , are shown in Table 2. It should be noted that small fluctuations in the cavity closure area are observed even though the solution stabilizes, and hence the upper and lower bound values of C_L and C_D should also be compared. As shown in Table 2, a temporal discretization of $\Delta t_f = 0.0001$

Table 1. Convergence of the lift and drag coefficients with number of elements for steady, subcavitating flow. $\sigma = 7$, $\alpha = 6^\circ$, $Re = 750,000$, $\Delta t_f = 0.0001$ s.

N_{foil}	N_{total}	C_L	(%)	C_D	(%)
100	17 527	0.9742	2.9	0.02145	20.4
130	29 093	0.9388	0.8	0.01900	6.6
230	56 552	0.9490	0.3	0.01801	1.1
400	126 021	0.9483	0.2	0.01769	0.7
$N_{max} = 680$	163 144	0.9464	-	0.01782	-

s, which corresponds to a mean Courant-Friedrichs-Lewy (CFL) number of $CFL = u\Delta t_f/\Delta x \lesssim 1$, is needed to reach convergence.

Table 2. Convergence of the lift and drag coefficients with time step size for steady, cavitating flow. $\sigma = 1.49$, $\alpha = 6^\circ$, $Re = 750,000$, $N_{foil} = 400$.

Δt_f (s)	C_L	C_D
10^{-3}	0.912 ± 0.1180	0.0282 ± 0.0062
5×10^{-4}	0.919 ± 0.0328	0.0276 ± 0.0041
10^{-4}	0.923 ± 0.0005	0.0278 ± 0.0001
5×10^{-5}	0.923 ± 0.0001	0.0278 ± 0.00002

2.4 FSI Coupling Algorithm

The foil displacement is applied after the fluid solution convergences for the fixed, rigid body problem. A schematic representation of the explicit, loose-coupling coupling between the CFD and 2-DOF models is shown in Figure 3. The explicit, loose-coupling method is used because the numerical results shown in this paper concerns only cases with steady cavitation. The FSI coupling algorithm involves calculating the L and T based on integration of the pressure and shear stresses on the foil surface, which are then used to compute h and θ via Eqns. 10 and 11. A user-defined subroutine is then used to update the foil boundary, and the entire fluid mesh is updated. To enhance convergence, the displacements are under-relaxed during the first 0.1 s of the coupled FSI calculation. The structure time step size, $\Delta t_s = 0.001$ s, is set to be 10 times the fluid time step size, $\Delta t_f = 0.0001$ s, to reduce remeshing/computational cost since it is not necessary to use such a fine time step size to capture the foil motion in the 2-DOF model. Only steady-state results are shown in this paper. Because small fluctuations of the cavity are observed between two successive time steps, the convergence criterion requires the change in the average values of h , θ , C_L , and C_D over 10 structure time steps normalized by the average values of the 10 previous time steps to be less than $1e^{-4}$.

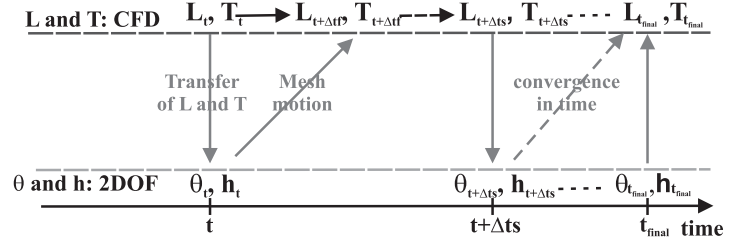


Figure 3. FSI coupling algorithm

3 Experimental Model

Experimental measurements of the hydrofoil described in the previous section were carried out in the cavitation tunnel at IRENav (French Naval Academy, France). The test section is 1 m long and has a 0.192 m x 0.192 m square section. The in-flow velocity can be varied between 0 and 15 m/s and the tunnel pressure can be varied between 30 mbar to 3 bar.

Two sets of experiments are investigated in this section, a rigid hydrofoil experiment and a flexible hydrofoil experiment. The rigid hydrofoil was made of stainless steel and the flexible hydrofoil was made of POM Polyacetate. Both sets of experiments were conducted in the same facility, and the initial undeformed geometries of both hydrofoils were made to be identical. Both subcavitating and cavitating flow conditions were investigated. The objective is to investigate FSI effects for both subcavitating and cavitating flow conditions by comparing the performance of the rigid and flexible hydrofoils.

3.1 Rigid Hydrofoil

The experimental setup for the rigid hydrofoil made of stainless steel is shown in Figure 4. The Young's modulus, density, and Poisson's ratio of stainless steel are respectively $E=210,000$ MPa, $\rho_s = 7,800$ kg/m³, and $\nu = 0.3$. The stainless steel hydrofoil was rigid enough such that the hydrodynamic load induced deformations were negligible. To measure the wall pressures, piezo-resistive pressure transducers were mounted into small cavities with 0.5 mm diameter pinholes drilled along the mid-span of the hydrofoil surface. The pressure transducers were set to measure pressures up to 10 bars, and the sampling frequency was set to 20 kHz. Lift and drag were also measured using a resistive gauge hydrodynamic balance with a range up to 150 daN in lift and 15 daN in drag. Readers should refer to Leroux et al 2005 [18] and Ducoin et al. 2009 [19] for additional details about the rigid hydrofoil experimental setup and results.

3.2 Flexible Hydrofoil

The experimental setup for the flexible hydrofoil made of POM Polyacetate is shown in Figure 5. The Young's modulus, density, and Poisson's ratio of POM Polyacetate are respectively

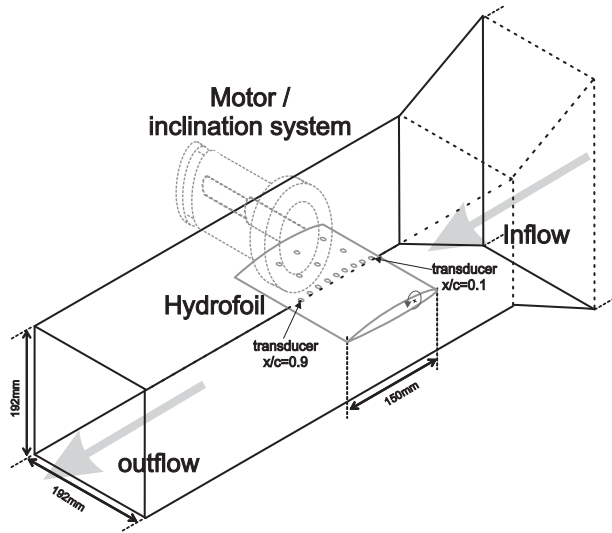


Figure 4. Experimental setup for the rigid hydrofoil.

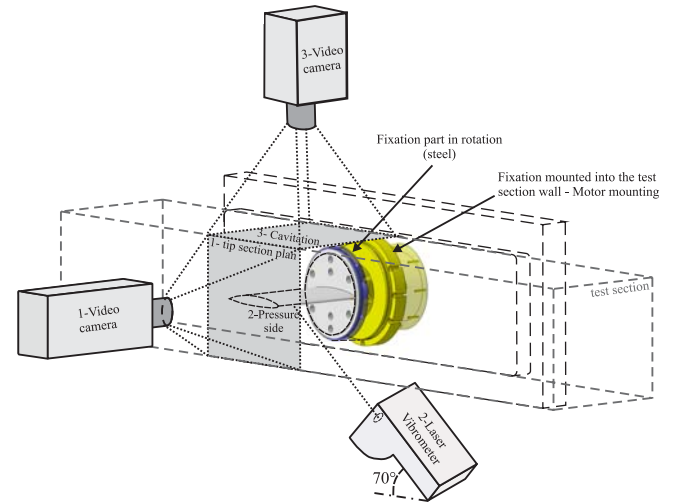


Figure 5. Experimental setup for the flexible hydrofoil.

$E=3,000$ MPa, $\rho_s = 1,480$ kg/m³, and $\nu = 0.35$. No pressure or force measurement was made for the rigid hydrofoil to avoid changes in stiffness and deformation characteristics due to the presence of the pressure transducers or load cells. The root section of the cantilevered hydrofoil was clamped to a steel cylindrical system linked to a motor to allow static or dynamic change in the angle of attack.

A high-speed video camera PHOTRON (camera 3 in Figure 5) set to a frequency of 2000 Hz was placed on top of the test section to observe the cavitation patterns on the suction side of the foil surface. A separate video camera BASLER (camera 1 in Figure 5) set to a frequency of 100 Hz was placed near the free end of the hydrofoil to measure the instantaneous tip displacements. A Laser Doppler Vibrometer (LDV) (camera 2 in Figure 5), Polytech PSV-400, was used to measure the structural vibrations with a sensitivity ranging between 10 mm/s/Volts to 1 m/s/Volts. The laser was fixed to the bottom of the tunnel test section to avoid reflection caused by the suction side cavitation. The experimental facility does not allow the laser to be set exactly perpendicular to the section and it was oriented at 70° from the test section wall. Readers should refer to [12] for more details about the flexible hydrofoil experimental setup and results.

4 Results and Discussions

4.1 Rigid Hydrofoil

To validate the fluid solver, numerical predictions are compared with experimental measurements for the rigid hydrofoil set at an angle of attack of $\alpha = 6^\circ$, $Re = 750,000$ for both subcavitating and cavitating conditions. The wall pressure data and force measurements with and without cavitation are taken from Leroux et al. 2004 [20]. Figure 6 shows that the predicted variations

of the pressure coefficients ($C_P = (P - P_\infty) / (0.5\rho_l V_\infty^2)$) along the normalized chord positions (X/c) compare well with experimental measurements for the case of subcavitating flow ($\sigma = 7$). The predicted lift coefficient of $C_{Lnum} = 0.94$ also compares well with the measured value of $C_{Lexp} = 0.91$.

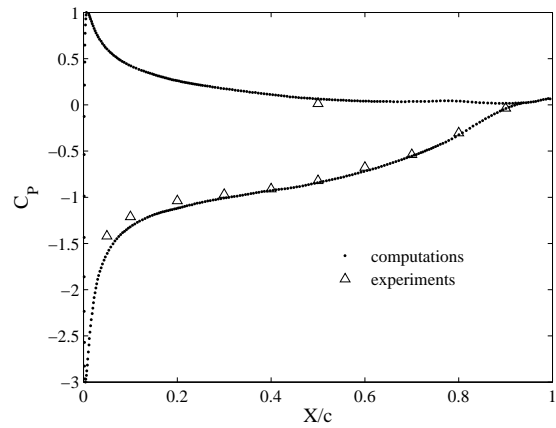


Figure 6. Computed versus measured pressure coefficient for the rigid hydrofoil in subcavitating flow. $Re = 750,000$, $V_\infty = 5$ m/s, $\alpha = 6^\circ$, $\sigma = 7$.

Figure 7 shows the cavitation patterns, represented by the volume fraction of vapor, predicted by the RANS solver for three different cavitation numbers ($\sigma=1.62$, 1.55, and 1.49). Stable, leading edge, sheet cavitation on the suction side is predicted for all three cases. As expected, the cavity length increases with decreasing cavitation number. The cavitation model predicts a small unsteady region at the cavity closure region, where the re-

entrant jet develops. This unsteady region tends to increase with increasing cavity length. This phenomenon was also observed during the experiments, and small shedding of the vapor structures were observed even for small cavities. The fluctuations increase with the growth of the cavity until fully unsteady sheet cavitation develops. Nevertheless, quasi-steady cavitation was observed for the three cases shown in Figure 7.

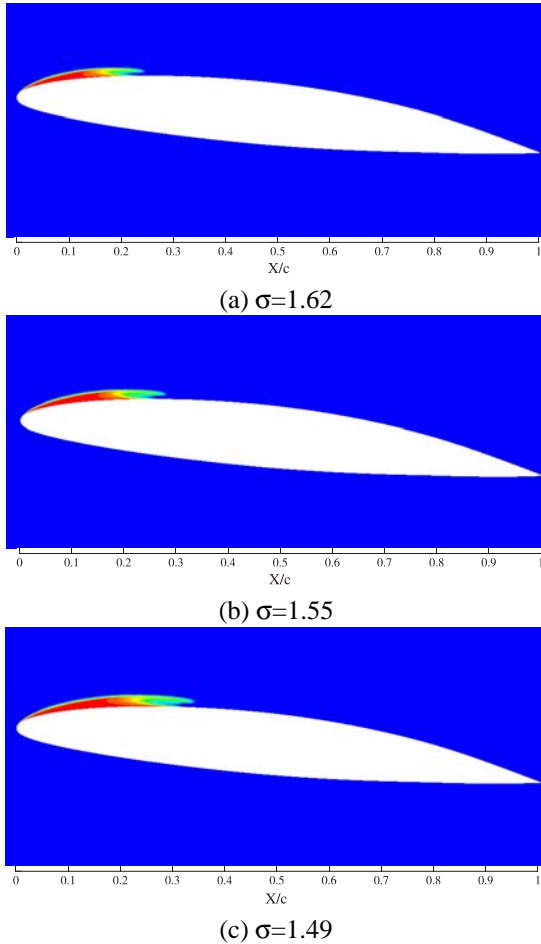


Figure 7. Predicted cavitation patterns as represented by the vapor volume fraction for the rigid hydrofoil at 3 different cavitation numbers , $Re = 750,000$, $V_\infty = 5$ m/s, $\alpha = 6^\circ$.

The computed pressure coefficients for the three cavitating cases are compared with the measured values in Figure 8. As expected, the pressure is constant in the cavitating region. The numerical predictions compare well with experimental measurements in the cavitating region and downstream of the cavity, although some differences are observed at the cavity closure region. The RANS solution seems to under-predict the cavity length about 10% to 20%. This may be because of the high vorticity predicted by the current model at the cavity

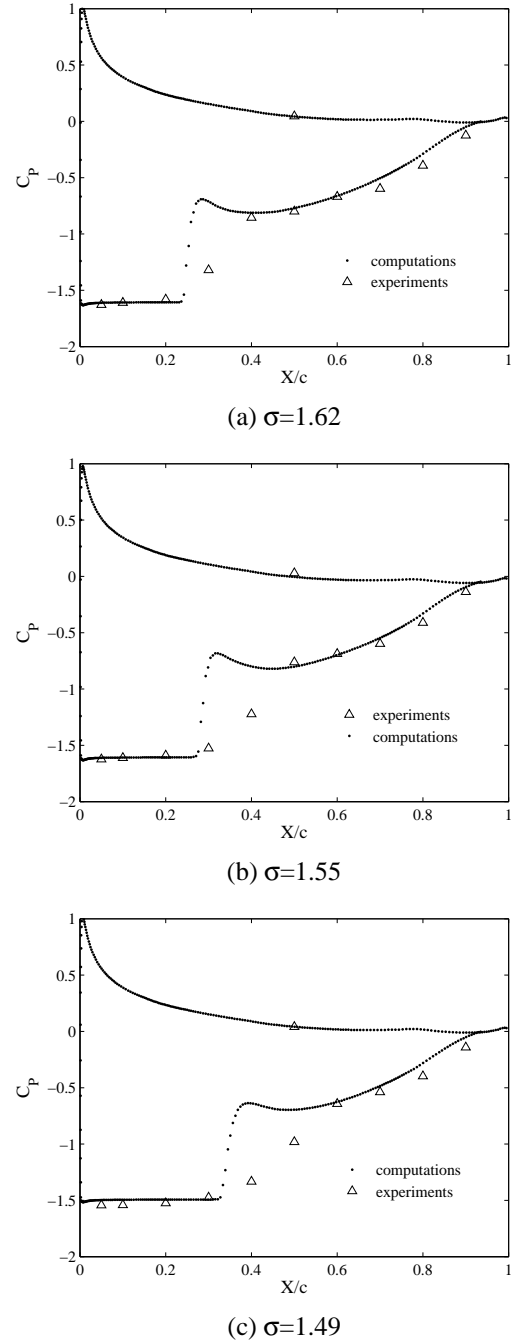


Figure 8. Comparison of the predicted and measured cavitating pressure coefficients for the rigid hydrofoil at 3 different cavitation numbers. $Re = 750,000$, $V_\infty = 5$ m/s, $\alpha = 6^\circ$.

closure region.

The hydrodynamic coefficients (C_L and C_D) and normalized cavity lengths (L_c/c) for various cavitation numbers, from in-

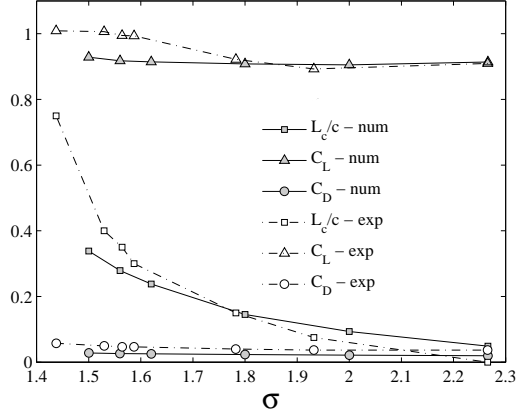


Figure 9. Comparisons of the predicted and measured normalized cavity lengths (L_c/c), lift and drag coefficients (C_L and C_D) of the rigid hydrofoil at various cavitation numbers. $Re = 750,000$, $V_\infty = 5$ m/s, $\alpha = 6^\circ$.

ception near $\sigma = 2.5$ to the limit value of $\sigma=1.49$ for stable cavitation, are shown in Figure 9. Good agreements are observed for cases with high cavitation number. The RANS solutions seem to under-predict the lift coefficient and cavity lengths for $\sigma < 1.8$. The predicted drag coefficients share the same trend as with experimental measurements although the numerical values are much lower than the measured values.

4.2 Flexible Hydrofoil

Results are shown in this section for the flexible hydrofoil at an angle of attack of $\alpha = 8^\circ$ and $Re = 750,000$. The values of the bending and the torsional stiffnesses are respectively $K_h = 130911$ N/m and $K_\theta = 2800$ Nm/rad. Two cavitation numbers of $\sigma = 2.6$ and $\sigma = 2.4$, corresponding to quasi-stable cavitation cases, are considered in this sub-section.

The convergence time history of the tip displacements and lift coefficient are first shown in Figure 10 and 11 for the case of cavitating flow with $\sigma = 2.4$. As mentioned in Section 2.4, coupled calculations initiates after the hydrodynamic solution converged for the rigid body problem, which occurs at $t = 1.9$ s for this case. Fluctuations can be observed when the foil is initially deformed, and then the solution stabilizes when $t \geq 2.15$ s. It should be noted that the small fluctuations observed for $t > 2.15$ s are associated with fluctuations of the cavity closure location.

Comparisons of the predicted hydrodynamic coefficients and cavity lengths for the rigid (C_{L-R} , C_{D-R} , L_{C-R}/c) and flexible (C_{L-F} , C_{D-F} , L_{C-F}/c) hydrofoils are summarized in Table 3. The results for the flexible case are obtained using the coupled FSI algorithm described in Section 2.4. For the rigid hydrofoil, the lift coefficient decreases and the drag coefficient increases with decreasing cavitation number. The lift and drag coefficients of the flexible hydrofoil are higher than the rigid foil for all three

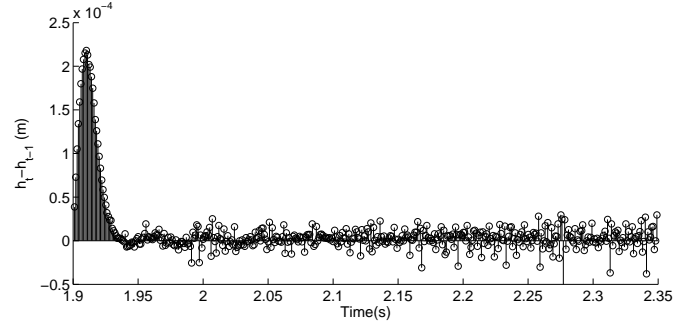


Figure 10. Convergence time history of the tip displacements (h) for the case of the flexible hydrofoil in cavitating flow. $\sigma = 2.4$, $\alpha = 8^\circ$, and $Re = 750,000$, $V_\infty = 5$ m/s.

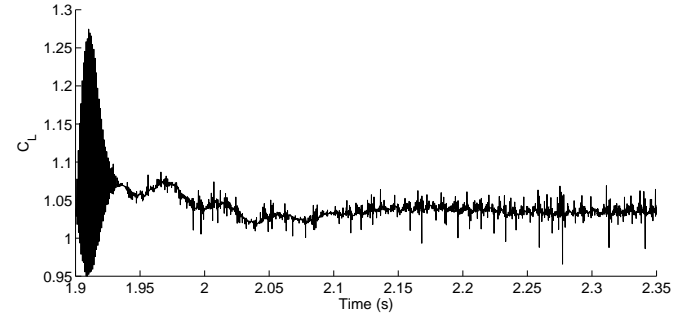


Figure 11. Convergence time history of the lift coefficient (C_L) for the case of the flexible hydrofoil in cavitating flow. $\sigma = 2.4$, $\alpha = 8^\circ$, and $Re = 750,000$, $V_\infty = 5$ m/s.

cases because the hydrodynamic loading leads to an increase in pitch (i.e. negative θ), and hence effective angle of attack. For all three cases, fluid-structure interaction lead to a higher increase in the drag coefficient compare to the increase in lift coefficient, which implies a lower efficiency. Stable cavitation was observed for all three cases. The predicted cavity lengths are longer for the flexible hydrofoil compared to the rigid hydrofoil because of the increase in effective angle of attack.

Table 3. Comparison of the predicted lift and drag coefficients, and normalized cavity length, for the rigid (subscript R) and flexible (subscript F) hydrofoils, and the twist angle (θ) for the flexible hydrofoil at three different cavitation numbers. $\alpha = 8^\circ$, $Re = 750,000$, $V_\infty = 5$ m/s.

σ	C_{L-R}	C_{D-R}	L_{C-R}/c	C_{L-F}	C_{D-F}	L_{C-F}/c	$\theta(^{\circ})$
7	1.168	0.0214	-	1.200	0.0228	-	-0.31
2.6	1.0346	0.0364	0.0667	1.0511	0.0413	0.09	-0.27
2.4	1.0313	0.0402	0.117	1.036	0.0441	0.123	-0.26

The predicted and measured values initial and deformed shape of the tip section of the flexible foil, and the corresponding predicted cavitation patterns, for the same three cavitation numbers are shown in Figure 12. Good agreements are found everywhere on the foil. The predicted maximum tip displacement and twist angle for the subcavitating flow case ($\sigma = 7$) are $\delta = 4.1$ mm and $\theta = -0.31^\circ$, respectively, compared with the measured value of $\delta = 3.4$ mm and $\theta = -0.4^\circ$. For $\sigma = 2.6$, the measured cavity length on the flexible hydrofoil is approximately 10% of the chord, where $\delta = 3.4$ mm and $\theta = -0.34^\circ$. In comparison, the predicted cavity length for the flexible hydrofoil is 9% of chord with $\delta = 3.6$ mm and $\theta = -0.27^\circ$ (while the cavity length for the rigid hydrofoil is 6.67% of chord, see Table 3). For $\sigma = 2.4$, the measured cavity length reached a mean value of 15% of the chord and is still stable; the corresponding measured tip displacements are $\delta = 3.5$ mm and $\theta = -0.28^\circ$. The predicted cavity length for the flexible hydrofoil is 12.3% of chord with $\delta = 3.5$ mm and $\theta = -0.26^\circ$ (while the cavity length for the rigid hydrofoil is 11.7% of chord). As expected, the coupled solution compared better with the measured value for the case of the flexible foil because it captures the increase in effective angle of attack caused by the fluid-structure interaction. Small shedding of the vapor structure was observed during the experiment for $\sigma = 2.4$ for the case of the flexible hydrofoil, but it was not captured in the computation.

For lower cavitation numbers, it was observed during the experiments that the cavities become unstable and detached completely for $\sigma < 2$, which was observed to formed cloud cavitation that convected to the wake. Fluctuations in tip displacements were also observed. Coupled FSI computations for cases with unsteady cavitation are currently underway.

Figure 13 shows the measured values of the spatially averaged velocity spectrum over the pressure side of the flexible hydrofoil for three different cavitation numbers at $\alpha = 8^\circ$. At $\sigma = 7$ (no cavitation), Figure 13 shows that the first four wetted resonance frequencies of the hydrofoil are excited by the attached flow around the hydrofoil. The structure is globally excited by the cavitating flow. The development of cavity along the hydrofoil chord and the presence of unsteady cavitation (see Figure 13 for $\sigma = 2.0$) have a strong effect on the vibrational responses, which increased globally with additional peaks around the first resonance mode. It should be noted that natural frequencies are also modified by the presence of vapor on the hydrofoil surface, see for example mode 4 on Figure 13. Coupled FSI computations to investigate the influence of cavitation dynamics on the vibrational characteristics are currently underway.

5 Conclusions

The hydroelastic behavior of a rigid and a flexible hydrofoil in turbulent subcavitating and cavitating flows are investigated in this work via combined numerical and experimental studies. The numerical computations for the flexible hydrofoil are obtained

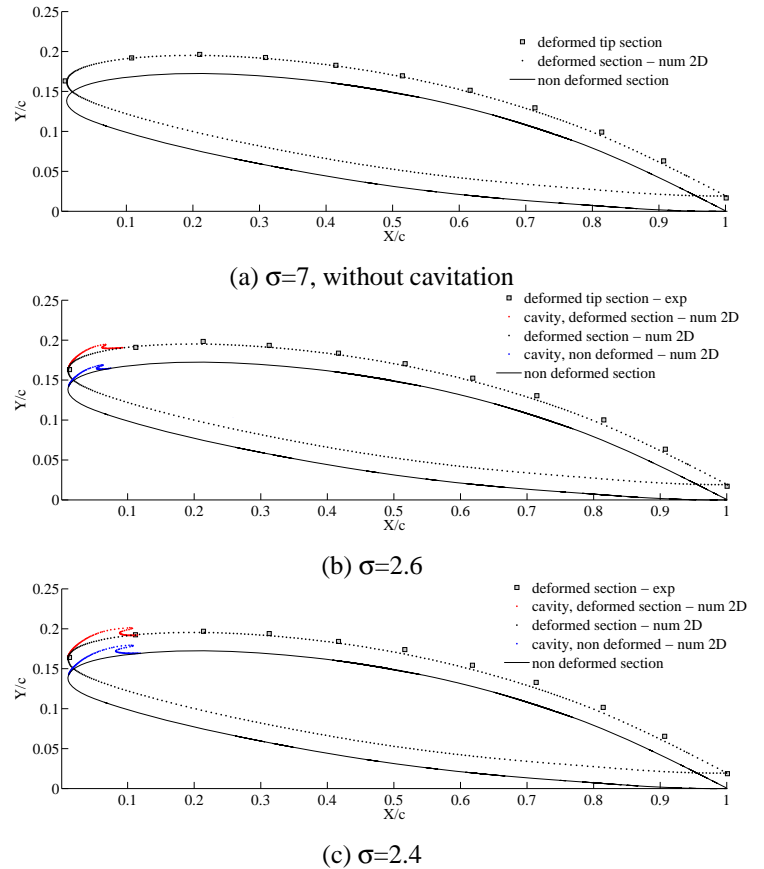


Figure 12. Comparisons of the measured and predicted displaced tip section for various cavitation numbers. Blue points are the predicted cavity contour for $\alpha_p = 0.5$, $Re = 750,000$, $V_\infty = 5$ m/s, $\alpha = 8^\circ$.

by coupling the commercial RANS solver, STAR-CCM+, with a 2-DOF model representing the tip section of the cantilevered, rectangular hydrofoil with plunging and pitching degrees of freedom. Comparisons between the numerical predictions and experimental measurements are shown for both rigid and flexible hydrofoils to identify the effects of fluid-structure interaction.

In general, good agreements were observed between the computations and measurements for both rigid and flexible hydrofoils in subcavitating and cavitating flow conditions. For the flexible hydrofoil made of POM polyacetate, both computations and measurements show that elastic deformations lead to increase in the effective angle of attack, which in turn lead to increases in lift and drag coefficients, decreases in lift to drag ratios, and increases in cavity lengths.

It should be noted that only cases with stable cavitation are shown in this work, and the numerical results are limited to those obtained via 2-D simulations. For cases with unsteady shedding of the cavities, significant interaction effects between the shedding frequencies and the foil natural frequencies were observed during the experiments. The presence of the cavitation on the hy-

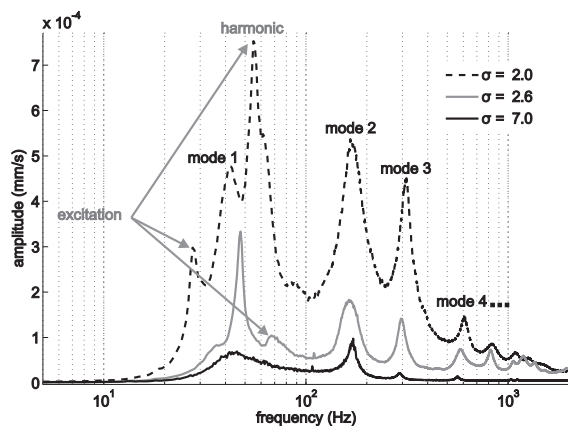


Figure 13. Measured velocity spectrum of the flexible hydrofoil at various cavitation number. $\alpha = 8^\circ$, $Re = 750,000$

drofoil also modified the natural frequencies because of changes in added mass effect due to transformation of water to vapor. Work is currently underway to compute the unsteady responses of the 3-D elastic hydrofoil in cavitating flow.

ACKNOWLEDGMENT

The authors gratefully acknowledge the IRENav and Prof. J.A. Astolfi for providing the experimental data on the rigid hydrofoil. The authors are also grateful to the Office of Naval Research (ONR) and Dr. Ki-Han Kim (program manager) for their financial support through grant numbers N00014-09-1-1204 and N00014-10-1-0170. The authors would also like to thank Dr. B.R. Savander for his help with STAR-CCM+.

REFERENCES

- [1] Arndt, R., 1981. "Cavitation in fluid machinery and hydraulic structures". *Annual Review of Fluid Mechanics*, **13**(1), pp. 273–326.
- [2] Brennen, C., 1995. *Cavitation and bubble dynamics*. Oxford University Press, USA.
- [3] Kuiper, G., 1997. "Cavitation Research and Ship Propeller Design". *Flow, Turbulence and Combustion*, **58**(1), pp. 33–50.
- [4] Laberteaux, K., and Ceccio, S., 2001. "Partial cavity flows. Part 1. Cavities forming on models without spanwise variation". *Journal of Fluid Mechanics*, **431**, pp. 1–41.
- [5] Callenaere, M., Franc, J., Michel, J., and Riondet, M., 2001. "The cavitation instability induced by the development of a re-entrant jet". *Journal of Fluid Mechanics*, **444**, pp. 223–256.
- [6] Kinnas, S., and Fine, N., 1993. "A numerical nonlinear analysis of the flow around two- and three-dimensional partially cavitating hydrofoils". *Journal of Fluid Mechanics*, **254**, pp. 151–181.
- [7] Senocak, I., and Shyy, W., 2002. "Evaluations of Cavitation Models for Navier-Stokes Computations". In FEDSM2002, July 14–18, Montreal, Quebec, Canada, ASME.
- [8] Gowing, S., Coffin, P., and Dai, C., 1998. "Hydrofoil cavitation improvements with elastically coupled composite materials". In Proceedings of 25th American towing tank conference, Iowa City, IA.
- [9] Young, Y., 2008. "Fluid-structure interaction analysis of flexible composite marine propellers". *Journal of Fluids and Structures*, **24**(6), pp. 799–818.
- [10] Motley, M., Liu, Z., and Young, Y., 2009. "Utilizing fluid-structure interactions to improve energy efficiency of composite marine propellers in spatially varying wake". *Composite Structures*, **90**(3), pp. 304–313.
- [11] Amromin, E., and Kovinskaya, S., 2000. "Vibration of Cavitating Elastic Wing in a Periodically Perturbed Flow: Excitation of Subharmonics". *Journal of Fluids and Structures*, **14**(5), pp. 735–751.
- [12] Ducoin, A., Deniset, F., Astolfi, J., and Sigrist, J., 2009. "Numerical and Experimental Investigation of Hydrodynamic Characteristics of Deformable Hydrofoils". *Journal of Ship Research*, **53**(4), pp. 214–226.
- [13] Spalart, P., and Allmaras, S., 1992. "A one-equation turbulence model for aerodynamic flows". In AIAA, Aerospace Sciences Meeting and Exhibit, 30th, Reno, NV, p. 1992.
- [14] Seo, J. H., and Lele, S. K., 2009. "Numerical investigation of cloud cavitation and cavitation noise on a hydrofoil section". In Proceedings of The 7th International Symposium on Cavitation (CAV 2009), August 17–22, Ann Arbor, Michigan, USA.
- [15] Jones, W., and Launder, B., 1972. "The Prediction of Laminarisation with a Two Equation Turbulence Model". *Int. J. Heat Mass Transfer*, **15**(2), pp. 301–314.
- [16] Menter, F. R., 1993. "Improved Two-Equation k-Turbulence Models for Aerodynamic Flows". *NASA Technical Memorandum*, **103975**, p. 34.
- [17] Sauer, J., and Schneer, G., 2001. "Physical and numerical modeling of unsteady cavitation dynamics". In IMCF-2001, New Orleans, USA, May 27–June 1.
- [18] Leroux, J. B., Coutier-Delgosha, O., and Astolfi, J. A., 2005. "A joint experimental and numerical study of mechanisms associated to instability of partial cavitation on two-dimensional hydrofoil". *Physics of Fluids*, **17**, p. 052101.
- [19] Ducoin, A., Astolfi, J., Deniset, F., and Sigrist, J., 2009. "Computational and experimental investigation of flow over a transient pitching hydrofoil". *European Journal of Mechanics/B Fluids*, **28**, pp. 728–743.
- [20] Leroux, J., Astolfi, J., and Billard, J., 2004. "An experimental study of unsteady partial cavitation". *Journal of Fluids Engineering (Transactions of the ASME)*, **126**(1), pp. 94–101.